

This document is the Accepted Manuscript version of a Published Work that appeared in final form in *Nano Letters*, copyright © 2019 American Chemical Society after peer review and technical editing by the publisher. To access the final edited and published work see: <https://doi.org/10.1021/acs.nanolett.9b03063>

**Please cite this article as:**

Assessing the Reversed Exponential Decay of the Electrical Conductance in Molecular Wires: The Undeniable Effect of Static Electron Correlation

Sara Gil-Guerrero, Ángeles Peña-Gallego, Nicolás Ramos-Berdullas, Ángel Martín Pendás, and Marcos Mandado, *Nano Letters* 2019 19 (10), 7394–7399

DOI: [10.1021/acs.nanolett.9b03063](https://doi.org/10.1021/acs.nanolett.9b03063)

**Copyright © 2019 American Chemical Society**

# Assessing the reversed exponential decay of the electrical conductance in molecular wires: The undeniable effect of static electron correlation

Sara Gil-Guerrero,<sup>†</sup> Ángeles Peña-Gallego,<sup>†</sup> Nicolás Ramos-Berdullas,<sup>†,‡</sup> Ángel Martín Pendás,<sup>\*,¶</sup> and Marcos Mandado<sup>\*,†</sup>

<sup>†</sup>*Department of Physical Chemistry, University of Vigo, Lagoas-Marcosende s/n, 36310, Vigo, Spain*

<sup>‡</sup>*Institute of Theoretical Chemistry, University of Vienna, Währinger Str. 17, 1090 Vienna, Austria*

<sup>¶</sup>*Department of Analytical and Physical Chemistry, University of Oviedo, Calle Julián Clavería 8, 33006, Oviedo, Spain*

E-mail: ampendas@uniovi.es; mandado@uvigo.es

## Abstract

An extraordinary new family of molecular junctions, inaccurately referred to as “anti-Ohmic” wires in the recent literature, has been proposed based on theoretical predictions. The unusual electron transport observed for these systems, characterized by a reversed exponential decay of their electrical conductance, might revolutionize the design of molecular electronic devices. This behavior, which has been associated with intrinsic diradical nature, is reexamined in this work. Since the diradical character

arises from a near-degeneracy of the frontier orbitals, the employment of a multireference approach is mandatory. CASSCF calculations on a set of nanowires based on polycyclic aromatic hydrocarbons (PAHs) demonstrate that, in the frame of an appropriate multireference treatment, the ground state of these systems shows the expected exponential decay of the conductance. Interestingly, these calculations do evidence a reversed exponential decay of the conductance, although now in several excited states. Similar results have been obtained for other recently proposed candidates to “anti-Ohmic” wires. These findings open new horizons for possible applications in molecular electronics of these promising systems.

## Keywords

anti-Ohmic, molecular junction, electron transport, multireference, diradical, topological insulator

Recent theoretical results in the field of molecular electronics have led to proposal of the existence of a new family of molecular nanowires with unusual properties, inaccurately referred to as “anti-Ohmic” systems.<sup>1–22</sup> The term Ohmic has been coined at macroscopic level, where for some materials, mainly metals, the current/voltage relation is linear, following the Ohm’s law. This proportionality is expected whenever the electrons’ mean free path, usually determined by electron-phonon interactions, is much smaller than the sample’s length. In this regime, the electrical conductance decays linearly with the length of the wire. Therefore, strictly speaking, wires constructed at molecular scale can be considered neither Ohmic nor anti-Ohmic. Normally, the charge transport efficiency of molecular wires, in which the electron transport is associated with non-resonant tunneling, decays exponentially with the length of the wire.<sup>23–25</sup> However, the above-mentioned novel compounds evidence an unexpected behavior, as their conductance increases with length. Although this reversed exponential decay of the electrical conductance with the length of the wire was explored by different groups many years ago,<sup>26–29</sup> a subsequent work of Tada and Yoshizawa<sup>15</sup> on nano-sized graphite sheets has recently revived the interest for this topic. Despite theorists have subsequently proposed a large number of model systems with reversed exponential decay, no experimental evidence of this behavior has been yet found. However, experimental measurements of the electrical conductance in anthracene oligomers do not agree with theoretical predictions. For these wires, the exponential decay parameter,  $\beta$ , was found to be positive and the HOMO-LUMO energy gap in long wires significantly large.<sup>30</sup>

Two common characteristics have been established<sup>2,14</sup> for a system to follow this reversed behavior. First, most of the wires with efficient transport are proposed to be oligomers with strong  $\pi$ -orbital conjugation. Second, the increase of conductance has been connected with a significant diradical character or the contribution of zwitterionic forms<sup>1,10,31</sup>, which in turn is related to a narrowing of the HOMO-LUMO gap. Both conditions are correlated, since the stabilization of the diradical structure is favored by aromaticity and a strong bond con-



jugation.

In a recent paper,<sup>5</sup> in which a set of quinoid systems were found to exhibit this reversed conductance/length behavior, an analogy was established between this character in molecular wires and the one-dimensional topological insulator (1D-TI) model of Su, Schrieffer and Heeger (SSH).<sup>32</sup> A chemical interpretation of 1D-TIs was recently proposed by Pendás *et al*<sup>33</sup> within the Hückel approach using polyacetylene as model. They demonstrated that, in 1D-TIs, the frontier orbitals are strongly localized at the edges, almost degenerated and far in energy from the valence and conduction bands, with the system being an insulator in the bulk and highly conducting at the edges. This is the case also for the quinoid structures,<sup>5</sup> which, as a paradigm of reversed exponential decay, exhibits all the properties associated with 1D-TIs at the molecular scale.

Once a consensus has been achieved about the crucial role that the narrowing of the HOMO-LUMO gap plays in the appearance of reverse exponential decay of the conductance, the sturdiness of the methodology employed by most authors in the field is to be questioned. As the frontier orbital energy gap decreases, a single-reference treatment is less and less appropriate reference for describing the system wavefunction, and recourse to multi-reference methods becomes mandatory, even if only a qualitatively correct treatment of the system is sought for. Although several authors have employed these methods to analyze the diradical character of the wires, these methodologies have not been extended to transmission calculations, wherein electron transport is almost invariably estimated by means of the Non-Equilibrium Green's Functions (NEGF) approach in combination with Density Functional Theory (DFT).<sup>34,35</sup> Exceptions to single-determinant methods are also found in the literature. For instance, Joachim *et al.* introduced the calculation of the electron transmission through the electron scattering matrix using a configuration interaction (CI) treatment.<sup>36,37</sup> This method is appropriate to analyze the effect of dynamic electron correlation, but not

enough to provide a satisfactory solution for systems with a very narrow HOMO-LUMO gap, where the static electron correlation is crucial. There have been also a number of efforts in the literature to address self-energy effects in the prediction of molecular conductance.<sup>38,39</sup> Again, being the effects we describe related to static, not dynamic correlation, they will no longer be discussed here. In this situation, multireference methods, such as Complete Active Space Self-Consistent Field (CASSCF) or Multireference Configuration Interaction (MRCI), are needed. Since preliminary CASSCF calculations on quinoid chains point to a complete quenching of the reverse exponential regime in the ground state, we believe that all the recently proposed candidates for “anti-Ohmic” behavior should be reviewed in light of these new results.<sup>1</sup>

According to this reasoning, a thorough study of some of these recently proposed systems is herein presented. In the body of this letter, we focus on nanowires based on polycyclic aromatic hydrocarbons (PAHs), comparing their conducting properties obtained from single- and multi-reference treatments. An equivalent analysis for some other proposed systems<sup>2,14</sup> is offered in the Supplementary Information (SI). These comprise molecular junctions formed by PAHs connected to gold leads by ethynylphenylthiol linkers, as well as cumulenes and quinoid-cumulenes moieties connected to gold by amine linkers. The conclusions reached for PAHs also hold for these other junctions.

Our results will prove that the orbital mixing and relaxation of occupied and virtual orbitals arising from the CASSCF treatment destroys the constructive interference that facilitate the electronic conduction in this type of molecular wires at DFT level. This does not depend a priori on the relative position of the Fermi level of the electrodes. The level alignment of the Fermi level will certainly change the relative value of the conductance for the different series of molecular wires investigated here, but it will not affect the conductance/length behavior within each series.

Firstly, carbon nanoribbons containing up to six fundamental units of naphthalene, anthracene, and tetracene were constructed following the scheme shown in Figure 1. The structures were optimized using DFT at the B3LYP/cc-pVDZ level, as implemented in the Gaussian 09 program.<sup>40</sup> Then the wavefunction stability was tested, finding that all the naphthalene structures from  $n = 1$  to  $n = 6$  units display a stable wavefunction. On the contrary, this is not the case in the anthracene- and tetracene-based systems, in which an instability unfolds for those structures with  $n > 2$  and  $n > 1$ , respectively. Reoptimization of the unstable structures in the triplet state sheds light on the origin of the instabilities, as they arise whenever the singlet-triplet gap is either about to close or even inverted (see Tables S1 and S2 of the SI).

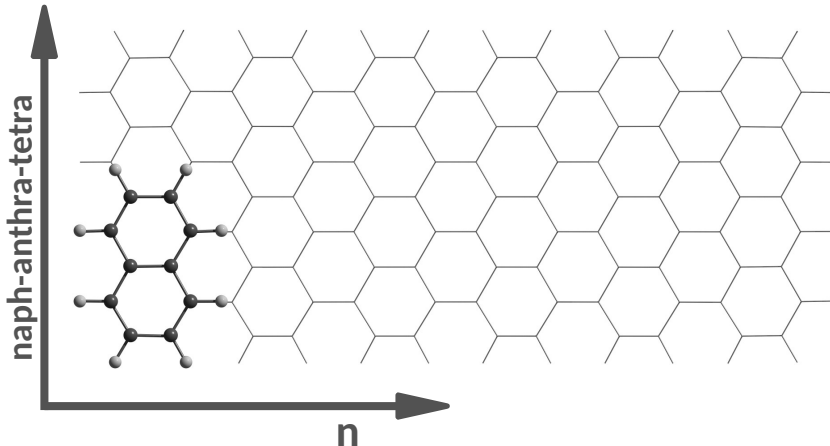


Figure 1: Schematic representation of the structure of the PAHs molecules studied in this work.

Given that multireference schemes are not yet available in standard NEGF-DFT implementations, an independent procedure able to extract the electrical conductance in molecular junctions at any level of theory is needed. In the context of the time-energy uncertainty approach, the electrical conductance can be explicitly obtained from electron transmission channels constructed from positive-negative pairs of Electron Deformation Orbitals (EDOs).<sup>41</sup> An in-house code (available upon request) has been used to obtain conductance for all the

proposed systems under the application of a bias voltage of 2V. For all the molecular junctions whose results are included in the SI, the electron transmission was calculated within the NEGF-DFT approach and compared to the conductance obtained from EDOs. In all cases, the same trends are found (see SI, Figures S5, S6, S14 and S15). The electrical conductance  $G$  for the PAHs is represented in Figure 2. Clearly,  $G$  increases with the size of the fundamental unit (tetracene > anthracene > naphthalene). In the anthracene and tetracene cases,  $G$  also increases with the number of units, whereas in naphthalene the conductance remains almost constant with the chain length. It can be observed how the trends are similar to those observed by Tada *et al* in nanosized graphene sheets.<sup>15</sup> Unfortunately, and importantly, we remark that it is in those structures in which the conductance is larger where the above-mentioned wavefunction instabilities appear.

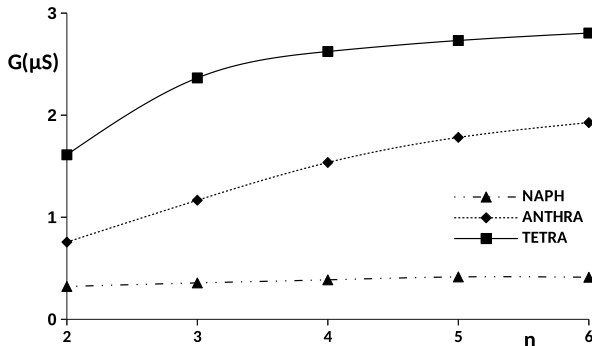


Figure 2: Evolution of the electrical conductance  $G$ , calculated within the EDOs formalism under a bias voltage of 2V, *vs* the number of fundamental units,  $n$ , in the PAHs.

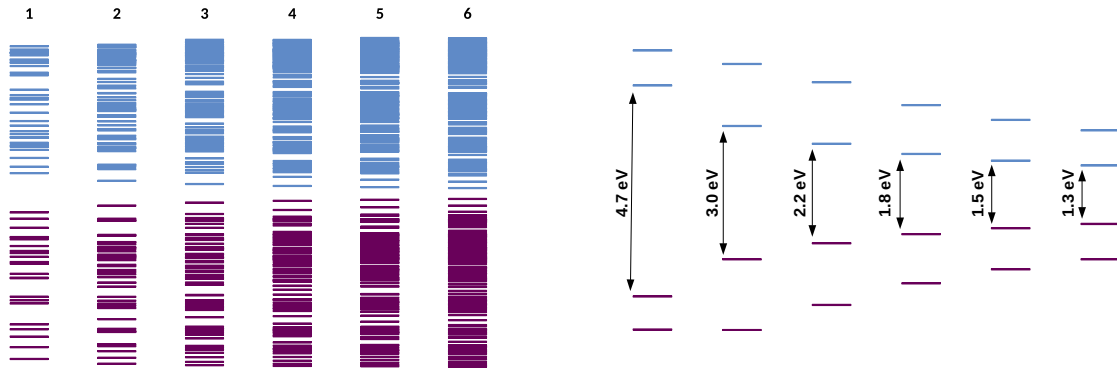
As stated, reversed exponential decay is found in systems where frontier orbitals are almost degenerate and distant energetically from the valence and conduction bands. This is easily corroborated in Figure 3, where orbital bands are represented. One can observe that the energy gap closes as the system grows, and that this phenomenon arises at shorter lengths when the fundamental unit is larger. Thus, as expected, when the HOMO-LUMO near-degeneracy condition is reached, the band representation shows two isolated orbitals in the middle of the gap between the conduction and valence bands and, in turn, the fron-

tier orbitals become extremely localized at the edges of the molecule, as can be observed in Figures S1-S3 of the SI. There is an unequivocal connection between orbital localization and high conductance, but also with the instability of the wavefunction.

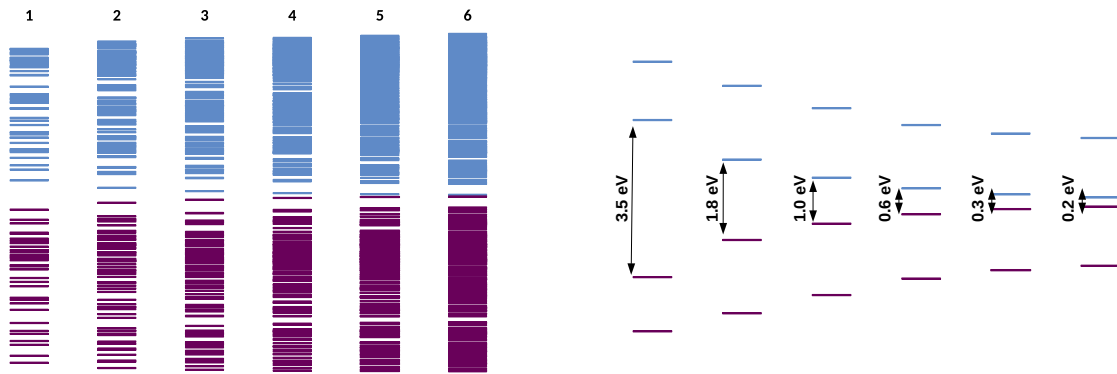
Orbital localization at the edges is also associated with a large long-range electron delocalization between them, and in turn to a strong electrical conductance. Martín Pendás *et al*<sup>42</sup> have shown how an atomic-pairwise additive partition of Resta’s<sup>43</sup> localization tensor (LT) is intimately linked to electrical conductivity (see SI for further details). In molecular wires, the decay rate of the edge-to-edge component of the LT controls the overall  $G$  value, so that with a single descriptor, that can be computed both in single- and multi-reference frameworks, the conductance of a given system can be qualitatively estimated.<sup>5</sup>

Figure 4 contains the DFT values of the interatomic LT component computed between the carbon atoms located at right- and left-hand sides of the PAHs as represented in Figure 1. Results for  $N = 1$ , obtained between covalently linked atoms and thus unrelated to long-range delocalization effects, have not been included. It can be observed that naphthalene-based wires display a subtle decrease of their LT with the number of units, although the LT never vanishes. In contrast, the edge-to-edge LT of anthracene and tetracene wires shows a very clear divergence with  $n$ , characteristic of conductive behavior and in agreement with our estimations of conductance. This will be used as a clear evidence of reversed exponential decay.

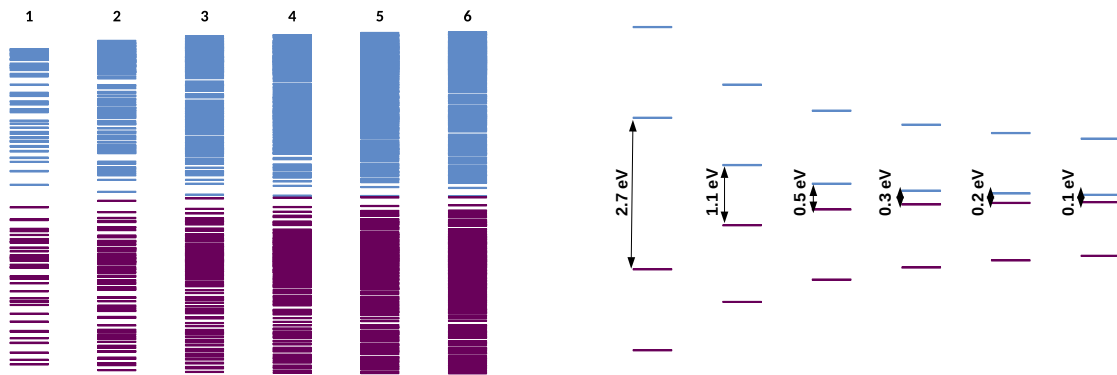
We now consider the effect of the above-mentioned HOMO-LUMO near-degeneracy, as well as the wavefunction instability, on the overall DFT conductance picture. To that end we must shift to a multireference scenario. Single-point calculations of the ground state of the PAHs studied in this work were performed using the CASSCF method as implemented in MOLCAS.<sup>44</sup> We have employed both the simplest possible (2,2) space that involves exclusively the HOMO and LUMO orbitals, and an extended (14,14) one. The (2,2) space



(a) Naphthalene



(b) Anthracene



(c) Tetracene

Figure 3: Kohn-Sham orbital bands of the PAHs containing from  $n = 1$  to  $n = 6$  units within an energy window spanning of  $(-0.9)-(0.5)$  au range

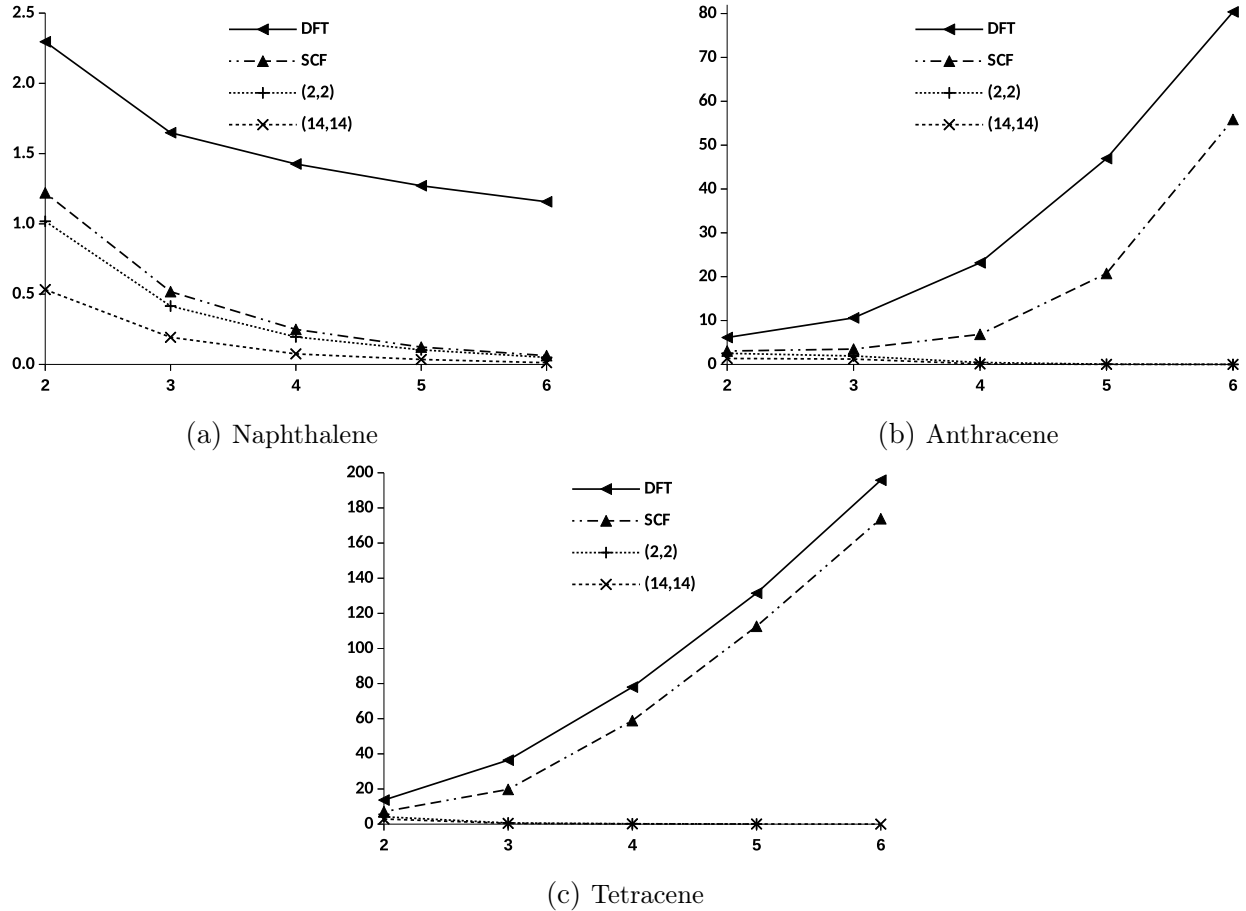


Figure 4: Evolution of the edge-to-edge interatomic localization tensor component ( $\Lambda^{AB}/au$ ) *vs* the number of fundamental units,  $n$ , in the PAHs.

is a good choice for the largest systems, where the HOMO and LUMO are far from the remaining virtual and occupied orbitals. Also, for smaller systems, the choice of a (14,14) active space is accurate enough according to previous studies.<sup>14</sup> These calculations show that the ground state of the naphthalene-based structures is mainly represented by the doubly occupied HOMO configuration. However, for the anthracene and tetracene series, it can be observed that the doubly occupied LUMO configuration gains weight as the number of units increases, until reaching almost equal weight for the largest structures (see Tables S3 and S4 of the SI). In order to analyze the effect of these results in the conductance of the system, the LT was calculated with the SCF, CASSCF(2,2) and CASSCF(14,14) levels and represented in Figure 4. It can be observed that, for naphthalene, inclusion of static correlation does not

alter the qualitative single-determinant LT picture, although the LT decay is now considerably faster. However, for anthracene and tetracene, while the SCF calculations follow a curve that is less steep than in DFT, but still rising with the number of units, for the CASSCF calculations the LT drops to zero rapidly. As mentioned before, for the largest systems in both the anthracene and tetracene series, the LT results obtained using the (2,2) and (14,14) active spaces are basically coincident. These findings show not only that the single-reference treatment of the reversed exponential decay has been probably erroneous so far, but also that the physical properties obtained from single-reference modeling are misleading. When a proper methodology is used, our results suggest that the electrical conductance of the ground state of these systems follows the common exponential decay with length.

However, the multireference scenario raises the possibility of finding the reversed exponential decay, not in the ground but in an excited state. We are examining here the possibility that a multireference excited state well isolated from the ground state might display the appropriate coherence properties that we have shown to be destroyed by static correlation in the ground state. Such a state might be accessed, for instance, via an optical excitation. Once the excited state has been reached, the application of a bias voltage would further mix it with other states and allow for electrical conductance. In order to prove this statement, State Average calculations were performed in the tetracene structures, since it is in these cases in which the LT evidences the most notable differences between the single- and the multireference scenario for the ground state. The smallest (2,2) space is reasonable enough to describe the first two excited states in the series. Within this simplified description, three possible singlet spin-adapted states are accessible, coming from the doubly occupied HOMO configuration  $|H\bar{H}| \equiv H^2$ , the doubly occupied LUMO  $|L\bar{L}| \equiv L^2$  one and, finally, from the equal, positive weight linear combination,  $1/\sqrt{2}(|H\bar{L}| + |\bar{H}L|) \equiv HL$ . It is well-known that for a 2-electron system the wavefunction may be expanded in Slater determinants constructed with natural spin orbitals.<sup>45</sup> The exact calculation of delocalization indices using



this form of the wavefunction was implemented previously.<sup>46</sup> Herein, we have employed the same methodology to calculate the LT within the 2-electron active space for the ground and excited states. The results are presented in Figure 5 and reflect the exponential decrease of the localization tensor with the number of tetracene units, previously discussed for the ground state (X), and the irregular increase in the case of the two excited states (S1 and S2) arising from the CASSCF(2,2) calculation. This irregular trend can be explained in the context of the change in the excited states along the tetracene series. The coefficients of the different configurations and the relative energies of the excited states are collected in Table S5 of the SI. In summary, the two excited states in the shortest systems are quite different and well-separated in energy, the lowest energy state (S1) corresponding to the singlet spin-adapted configuration HL, whereas the highest energy state (S2) corresponds to a combination of  $L^2$  and  $H^2$  with a significantly larger contribution from  $L^2$ . S2 follows the same trend as X for the structures with  $n=2$  and  $n=3$ , whereas in S1 the LT is significantly larger and increases with  $n$ . For  $n=4$ , the nature of the excited states changes completely, becoming a combination of the three spin-adapted configurations and giving rise to quasi-degenerate states for  $n \geq 4$ . As it can be seen in Figure 5, the LTs of S1 and S2 become quite similar at  $n=4$ , and increase gradually for  $n > 4$  with almost identical values for the two states. These results clearly indicate that large PAHs may display reversed exponential decay not in the ground state but in some of the lowest-energy excited states.

In conclusion, we believe that the results shown in this letter call into question the reversed exponential decay of the electrical conductance in molecular wires, at least in their ground state. We believe that the alleged exceptional electrical properties of recently proposed molecular systems have been predicted with methods that cannot tackle degeneracies or near degeneracies. In the context of a single-determinant procedure, such as that implemented in standard DFT, the electron transmission ability of these systems had already been linked with their diradical nature and to the vanishing of their HOMO-LUMO gap. In these

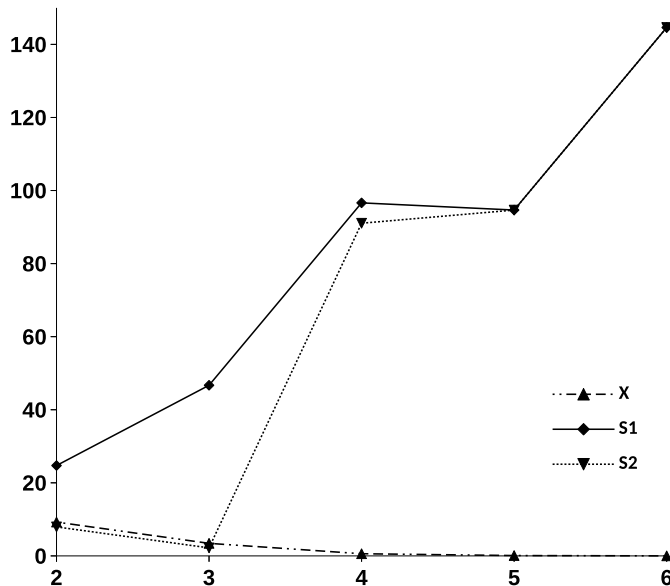


Figure 5: Evolution of the CASSCF(2,2) edge-to-edge interatomic localization tensor component ( $\Lambda^{AB}/au$ ) *vs* the number of fundamental units,  $n$ , in the tetracene series. The first three singlet states are shown (X, S1, S2).

circumstances, multireference calculations should take over, and in fact they show that the diradical character leads to a normal exponential decay of the conductance with the length of the chain in ground states, although reversed exponential decay is still found, this time in low lying excited states. Our results warn against the blind use of standardized methods in the field of molecular electronics, while opening new avenues in fields like optoelectronics, where this type of wires might well have a chance to be experimentally proven.

## Acknowledgements

S.G., A.P. and M.M. thanks Xunta de Galicia for financial support through the project GRC2019/24. N.R-B. thanks Xunta de Galicia for a postdoctoral grant. A.M.P. thank the spanish Ministerio de Ciencia, Innovación y Universidades for the grant PGC2018-095953-B-I00.

## References

- (1) Gil-Guerrero, S.; Ramos-Berdullas, N.; Mandado, M. *Org. Electron.* **2018**, *61*, 177–184.
- (2) Garner, M. H.; Bro-Jørgensen, W.; Pedersen, P. D.; Solomon, G. C. *J. Phys. Chem. C* **2018**, *122*, 26777–26789.
- (3) Algethami, N.; Sadeghi, H.; Sangtarash, S.; Lambert, C. J. *Nano Lett.* **2018**, *18*, 4482–4486.
- (4) Chen, W.; Li, H.; Widawsky, J. R.; Appayee, C.; Venkataraman, L.; Breslow, R. *J. Am. Chem. Soc.* **2014**, *136*, 918–920.
- (5) Gil-Guerrero, S.; Ramos-Berdullas, N.; Martín Pendás, Á.; Francisco, E.; Mandado, M. *Nanoscale Advances* **2019**, *1*, 1901–1913.
- (6) Li, S.; Gan, C. K.; Son, Y.-W.; Feng, Y. P.; Quek, S. Y. *Carbon* **2014**, *76*, 285–291.
- (7) Mahendran, A.; Gopinath, P.; Breslow, R. *Tetrahedron Lett.* **2015**, *56*, 4833–4835.
- (8) Ramos-Berdullas, N.; Ferro-Costas, D.; Mandado, M. *Comput. Theor. Chem.* **2015**, *1053*, 263–269.
- (9) Ramos-Berdullas, N.; Graña, A. M.; Mandado, M. *Theor. Chem. Acc.* **2015**, *134*, 20.
- (10) Ramos-Berdullas, N.; Mandado, M. *Chem.: Eur. J.* **2013**, *19*, 3646–3654.
- (11) Stuyver, T.; Fias, S.; De Proft, F.; Geerlings, P. *Chem. Phys. Lett.* **2015**, *630*, 51–56.
- (12) Stuyver, T.; Fias, S.; De Proft, F.; Geerlings, P.; Tsuji, Y.; Hoffmann, R. *J. Chem. Phys.* **2017**, *146*, 092310.
- (13) Stuyver, T.; Zeng, T.; Tsuji, Y.; Fias, S.; Geerlings, P.; De Proft, F. *J. Phys. Chem. C* **2018**, *122*, 3194–3200.

- (14) Stuyver, T.; Zeng, T.; Tsuji, Y.; Geerlings, P.; De Proft, F. *Nano Lett.* **2018**, *18*, 7298–7304.
- (15) Tada, T.; Yoshizawa, K. *J. Phys. Chem. B* **2004**, *108*, 7565–7572.
- (16) Tsuji, Y.; Movassagh, R.; Datta, S.; Hoffmann, R. *ACS Nano* **2015**, *9*, 11109–11120.
- (17) Valkenier, H.; Guédon, C. M.; Markussen, T.; Thygesen, K. S.; van der Molen, S. J.; Hummelen, J. C. *Phys. Chem. Chem. Phys.* **2014**, *16*, 653–662.
- (18) Tada, T.; Yoshizawa, K. *Phys. Chem. Chem. Phys.* **2015**, *17*, 32099–32110.
- (19) Sedghi, G.; Esdaile, L. J.; Anderson, H. L.; Martin, S.; Bethell, D.; Higgins, S. J.; Nichols, R. J. *Adv. Mater.* **2012**, *24*, 653–657.
- (20) Li, Z.; Park, T.-H.; Rawson, J.; Therien, M. J.; Borguet, E. *Nano Lett.* **2012**, *12*, 2722–2727.
- (21) Sedghi, G.; García-Suárez, V. M.; Esdaile, L. J.; Anderson, H. L.; Lambert, C. J.; Martín, S.; Bethell, D.; Higgins, S. J.; Elliott, M.; Bennett, N.; Macdonald, J. E.; Nichols, R. J. *Nat. Nanotechnol.* **2011**, *6*, 517–523.
- (22) Sedghi, G.; Sawada, K.; Esdaile, L. J.; Hoffmann, M.; Anderson, H. L.; Bethell, D.; Haiss, W.; Higgins, S. J.; Nichols, R. J. *J. Am. Chem. Soc.* **2008**, *130*, 8582–8583.
- (23) Winkler, J. R.; Gray, H. B. *J. Am. Chem. Soc.* **2014**, *136*, 2930–2939.
- (24) McCreery, R. L.; Bergren, A. J. *Adv. Mater.* **2009**, *21*, 4303–4322.
- (25) Ho Choi, S.; Kim, B.; Frisbie, C. D. *Science* **2008**, *320*, 1482–1486.
- (26) Reimers, J.; Hush, N. *Chem. Phys.* **1989**, *134*, 323 – 354.
- (27) Reimers, J.; Hush, N. *J. Photochem. Photobio. A* **1994**, *82*, 31 – 46.
- (28) Joachim, C. *Chem. Phys.* **1987**, *116*, 339 – 349.

- (29) Joachim, C.; Magoga, M. *Chem. Phys.* **2002**, *281*, 347 – 352.
- (30) Koch, M.; Ample, F.; Joachim, C. H.; Grill, L. *Nat. Nanotechnol.* **2012**, *7* 11, 713–720.
- (31) Morikawa, T.; Narita, S.; Klein, D. J. *Chem. Phys. Lett.* **2005**, *402*, 554–558.
- (32) Su, W. P.; Schrieffer, J. R.; Heeger, A. J. *Phys. Rev. Lett.* **1979**, *42*, 1698–1701.
- (33) Martín Pendás, Á.; Contreras-García, J.; Pinilla, F.; Mella, J. D.; Cárdenas, C.; Muñoz, F. A Chemical Theory of Topological Insulators. 28.01.2019; [https://chemrxiv.org/articles/A\\_Chemical\\_Theory\\_of\\_Topological\\_Insulators/7637009/1](https://chemrxiv.org/articles/A_Chemical_Theory_of_Topological_Insulators/7637009/1).
- (34) Herrmann, C.; Solomon, G. C.; Subotnik, J. E.; Mujica, V.; Ratner, M. A. *J. Chem. Phys.* **2010**, *132*, 024103.
- (35) Deffner, M.; Gross, L.; Steenbock, T.; Voigt, B. A.; Solomon, G. C.; Herrmann, C. ARTAIOS - a transport code for postprocessing quantum chemical electronic structure calculations, available from <https://www.chemie.uni-hamburg.de/ac/herrmann/software/index.html>.
- (36) Portais, M.; Joachim, C. *Chem. Phys. Lett.* **2014**, *592*, 272 – 276.
- (37) Portais, M.; Hliwa, M.; Joachim, C. *Nanotechnology* **2016**, *27*, 034002.
- (38) Strange, M.; Rostgaard, C.; Häkkinen, H.; Thygesen, K. S. *Phys. Rev. B* **2011**, *83*, 115108.
- (39) Darancet, P.; Ferretti, A.; Mayou, D.; Olevano, V. *Phys. Rev. B* **2007**, *75*, 075102.
- (40) Frisch, M. J.; Trucks, G. W.; Schlegel, H. B.; Scuseria, G. E.; Robb, M. A.; Cheeseman, J. R.; Scalmani, G.; Barone, V.; Petersson, G. A.; Nakatsuji, H.; et al., Gaussian 09. 2009.

- (41) Ramos-Berdullas, N.; Gil-Guerrero, S.; Mandado, M. *Int. J. Quantum Chem.* **2018**, *118*, e25651.
- (42) Pendás, Á. M.; Guevara-Vela, J. M.; Crespo, D. M.; Costales, A.; Francisco, E. *Phys. Chem. Chem. Phys.* **2017**, *19*, 1790–1797.
- (43) Resta, R.; Sorella, S. *Phys. Rev. Lett.* **1999**, *82*, 370–373.
- (44) Aquilante, F.; Autschbach, J.; Carlson, R. K.; Chibotaru, L. F.; Delcey, M. G.; DeVico, L.; Fdez. Galván, I.; Ferré, N.; Frutos, L. M.; Gagliardi, L.; et al., Open Molcas 8. *J. Comp. Chem.* **2015**, *37*, 506–541.
- (45) Shull, H.; Löwdin, P. *J. Chem. Phys.* **1956**, *25*, 1035–1040.
- (46) Mandado, M. *Theor. Chem. Acc.* **2013**, *132*, 1364.

# SUPPLEMENTARY INFORMATION

## Assessing the reversed exponential decay of the electrical conductance in molecular wires: The undeniable effect of static electron correlation

Sara Gil-Guerrero<sup>1</sup>, Ángeles Peña-Gallego<sup>1</sup>, Nicolás Ramos-Berdullas<sup>1,2</sup>, Ángel Martín Pendás<sup>\*3</sup> and Marcos Mandado<sup>\*1</sup>

<sup>1</sup>*Department of Physical Chemistry, University of Vigo, Lagoas-Marcosende s/n, 36310, Vigo, Spain; \*E-mail: mandado@uvigo.es*

<sup>2</sup>*Institute of Theoretical Chemistry, University of Vienna, Währinger Str. 17, 1090 Vienna, Austria*

<sup>3</sup>*Department of Analytical and Physical Chemistry, University of Oviedo, Calle Julian Clavería 8, 33006, Oviedo, Spain; \*E-mail: ampendas@uniovi.es*

## 1 Abbreviations

X-PAH <sub>n</sub>	Polycyclic Aromatic Hydrocarbons Fundamental units: X ∈ {naphthalene (N), anthracene (A), tetracene (T)} Number of fundamental units: $n \in \{1,2,3,4,5,6\}$
X-PAH <sub>n</sub> -Et	Polycyclic Aromatic Hydrocarbons + Ethynylphenylthiol linkers Fundamental units: X ∈ {naphthalene (N), anthracene (A), tetracene (T)} Number of fundamental units: $n \in \{1,2,3\}$
X-PAH <sub>n</sub> -Et-Au	Polycyclic Aromatic Hydrocarbons + Ethynylphenylthiol linkers + Gold Atom as Electrode Fundamental units: X ∈ {naphthalene (N), anthracene (A), tetracene (T)} Number of fundamental units: $n \in \{1,2,3\}$
Cum <sub>n</sub>	Cumulene Number of bonds (see Figure S12): $n \in \{1,2,3,4,5,6,7,8,9\}$
Cum <sub>n</sub> -Am	Cumulene + Amine linkers Number of bonds (see Figure S12): $n \in \{1,2,3,4,5,6,7,8,9\}$
Cum <sub>n</sub> -Am-Au	Cumulene + Amine linkers + Gold Atom as Electrode Number of bonds (see Figure S12): $n \in \{1,2,3,4,5,6,7,8,9\}$
QDC <sub>n</sub>	Quinoid-cumulenes Number of bonds (see Figure S13): $n \in \{1,2,3,4,5\}$
QDC <sub>n</sub> -Am	Quinoid-cumulenes + Amine linkers Number of bonds (see Figure S13): $n \in \{1,2,3,4,5\}$
QDC <sub>n</sub> -Am-Au	Quinoid-cumulenes + Amine linkers + Gold Atom as Electrode Number of bonds (see Figure S13): $n \in \{1,2,3,4,5\}$

## 2 Electrical conductivity and the Localization tensor (LT)

Although electrical conductivity in nanowires is usually accounted for within the non-equilibrium Green’s function (NEGF) approach, a ground state treatment of electrical conductivity exists after Kohn’s theory of the insulating state<sup>3</sup> and its modern reformulation by Vanderbilt and Resta.<sup>4</sup> These authors showed that insulators and conductors can be differentiated by an observable, the localization tensor (LT, or  $\lambda$ ), which diverges in conductors while converging in insulators:

$$\lambda = \frac{1}{N} \left\{ \langle \Psi | \hat{\mathbf{R}} \otimes \hat{\mathbf{R}} | \Psi \rangle - \langle \Psi | \hat{\mathbf{R}} | \Psi \rangle \otimes \langle \Psi | \hat{\mathbf{R}} | \Psi \rangle \right\}.$$

Unlike the standard implementation of NEGF in the DFT approach, which is usually restricted to single-configuration descriptions, the LT can be calculated for both single- and multi-reference states, providing a unique descriptor of electrical conduction in both finite and extended systems. The LT can be partitioned into intra- and interatomic contributions, and it can be shown<sup>5</sup> that its divergence is due, exclusively, to the decay rate of the interatomic terms with distance. Simply speaking, for a nanowire to be conductive the lead-to-lead component of the LT must diverge. As shown in a previous paper,<sup>6</sup> although a sensible definition of an atomic region (like that provided by the quantum theory of atoms in molecules) is needed to provide consistent LT values for small interatomic separations, these requirements smooth out at large distances, where essentially the same results are found with any partition, including that of Mulliken which is used here. As noticed in the main text, it is found that the DFT-LT may display a qualitatively incorrect behavior in multireference cases.

## 3 X-PAH<sub>n</sub>

### 3.1. Wavefunction stability and energy differences between singlet and triplet states

The wavefunction stability of the optimized X-PAH<sub>n</sub> treated in the body of the letter are collected in Table S1. In Table S2 we also report the triplet-singlet state energy differences.

Table S1: Stability (S) or Instability (I) of the wavefunction calculated at the B3LYP/cc-pVDZ level for X-PAH<sub>n</sub>

<i>n</i>	1	2	3	4	5	6
naphthalene (N)	S	S	S	S	S	S
anthracene (A)	S	S	I	I	I	I
tetracene (T)	S	I	I	I	I	I

Table S2: Triplet-singlet splitting (in kcal/mol) for X-PAH<sub>n</sub> calculated at the B3LYP/cc-pVDZ level

<i>n</i>	1	2	3	4	5	6
naphthalene (N)	62.27	34.48	22.75	16.20	11.93	8.86
anthracene (A)	41.51	12.15	-1.00	-8.42	-12.52	-14.57
tetracene (T)	27.46	-1.67	-12.29	-15.90	-17.17	-17.51



### 3.2. Kohn-Sham frontier orbitals representation

The Kohn-Sham HOMO-LUMO orbitals of all the X-PAH<sub>n</sub> are shown in Figures S1-S3.

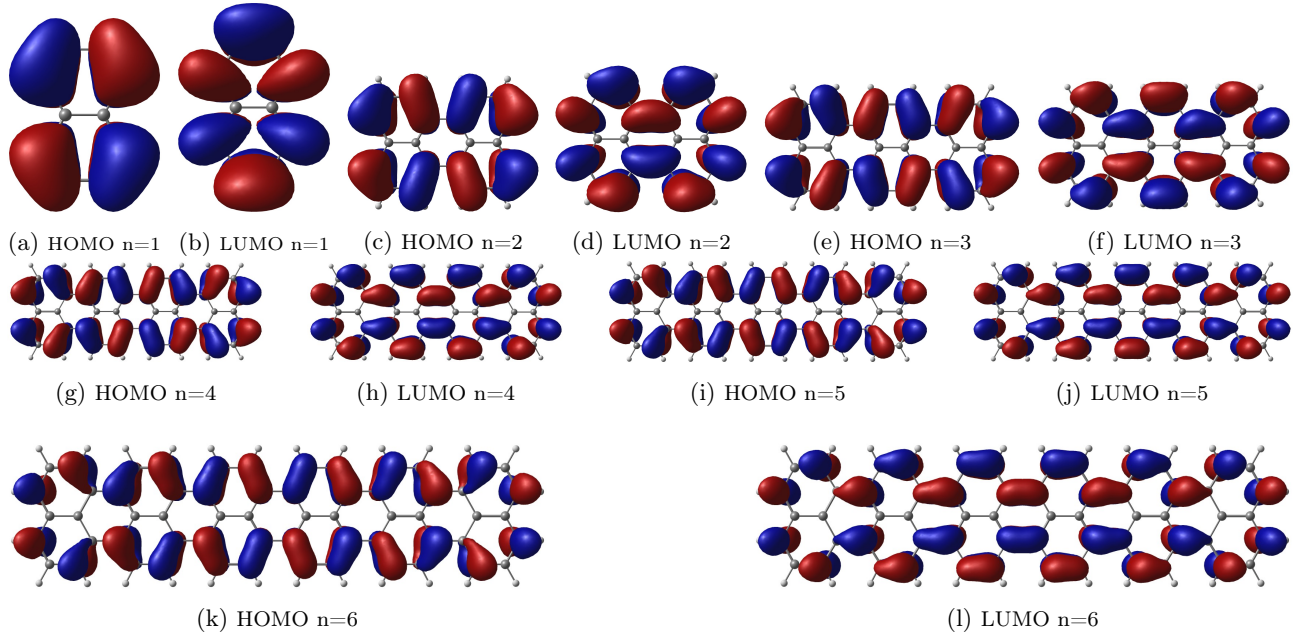


Figure S1: Kohn-Sham frontier orbitals of N-PAH<sub>n</sub>, Isosurface value=0.02

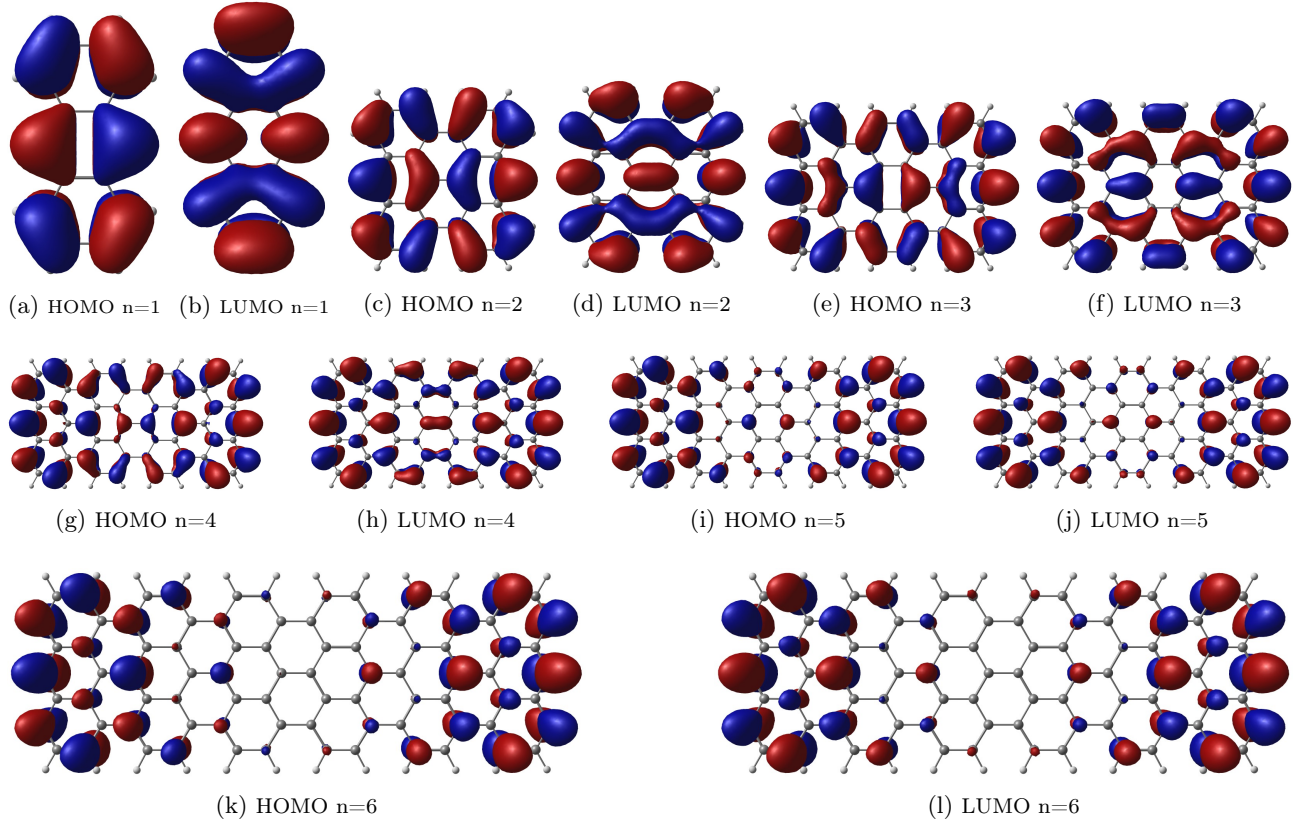


Figure S2: Kohn-Sham frontier orbitals of A-PAH<sub>n</sub>, Isosurface value=0.02

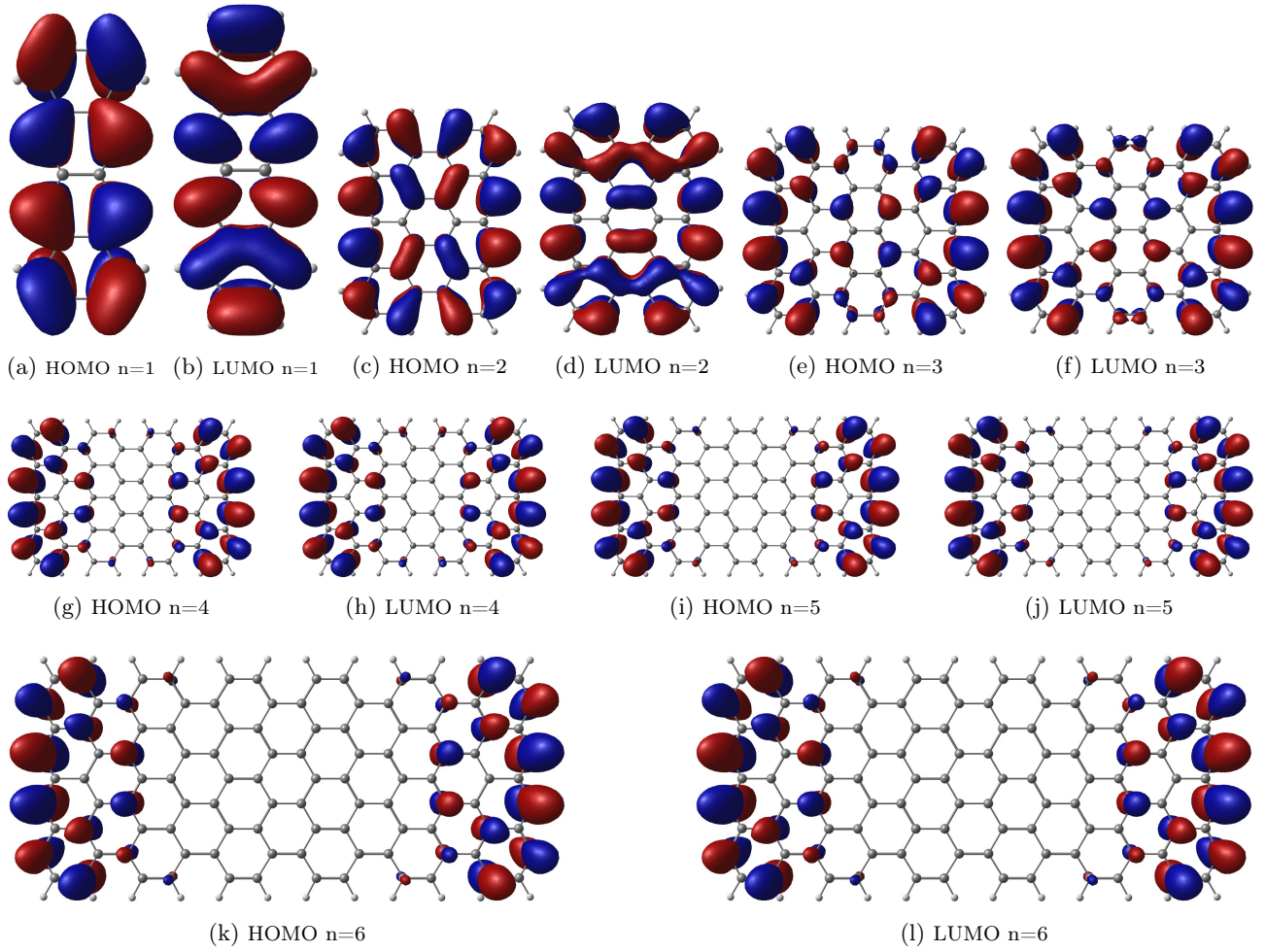


Figure S3: Kohn-Sham frontier orbitals of T-PAH<sub>n</sub>, Isosurface value=0.02

### 3.3. Complete Active Space Self Consistent Field (CASSCF) calculations

Single point (SP) calculations of the ground state (X) were performed at the CASSCF(14,14)/cc-pVDZ and CASSCF(2,2)/cc-pVDZ level of theory for all X-PAH<sub>n</sub> structures optimized at DFT level. Table S3 and Table S4 contain the relative weights of the most crucial configurations. It can be observed that, for those systems in which the wavefunction was found unstable at the DFT level, both the doubly occupied HOMO ( $H^2$ ) and the doubly occupied LUMO ( $L^2$ ) configurations are relevant.

Also, state average (SA) calculations in the three first singlet states (X, S1 and S2) were performed at the CASSCF(2,2)/cc-pVDZ level of theory for T-PAH<sub>n</sub> series. Table S5 contains the coefficients of the three possible singlet spin-adapted states: coming from the doubly occupied HOMO configuration  $|H\bar{H}| \equiv H^2$ , the doubly occupied LUMO  $|\bar{L}\bar{L}| \equiv L^2$  one and, finally, from the equal, positive weight linear combination,  $1/\sqrt{2}(|H\bar{L}| + |\bar{H}L|) \equiv HL$ .

Table S3: Weight of the ( $H^2$ ) and ( $L^2$ ) configurations of state X at CASSCF(2,2) of X-PAH<sub>n</sub>

$n$	1	2	3	4	5	6
naphthalene (N)						
$H^2$	0.97053	0.97139	0.97327	0.97390	0.97302	0.97457
$L^2$	0.02947	0.02861	0.02673	0.02610	0.02698	0.02543
anthracene (A)						
$H^2$	0.96521	0.96805	0.88386	0.58148	0.51893	0.50505
$L^2$	0.03479	0.03195	0.11614	0.41852	0.48107	0.49495
tetracene (T)						
$H^2$	0.96030	0.84856	0.54972	0.50824	0.50166	0.50037
$L^2$	0.03970	0.15144	0.45028	0.49176	0.49834	0.49963

Table S4: Weight of the ( $H^2$ ) and ( $L^2$ ) configurations of state X at CASSCF(14,14) of X-PAH<sub>n</sub>

$n$	1	2	3	4	5	6
naphthalene (N)						
$H^2$	0.8394	0.7665	0.77105	0.7758	0.78205	0.79297
$L^2$	0.01832	0.01618	0.00893	0.0136	0.00452	0.0073
anthracene (A)						
$H^2$	0.81206	0.76366	0.78238	0.40539	0.4273	0.41154
$L^2$	0.01843	0.02078	0.01233	0.34431	0.41098	0.40719
tetracene (T)						
$H^2$	0.7429	0.64345	0.42025	0.40134	0.43881	0.43095
$L^2$	0.01906	0.11687	0.36733	0.39297	0.43649	0.43049

Table S5: Coefficients of the ( $H^2$ ), (HL) and ( $L^2$ ) configurations for the X, S1 and S2 states at CASSCF(2,2) for T-PAH<sub>n</sub>

$n$	1	2	3	4	5	6
X						
$H^2$	0.98906	0.96026	0.82094	0.72349	0.70891	0.70732
HL	0.00000	-0.00002	-0.00004	0.00003	-0.00004	0.00000
$L^2$	-0.14751	-0.27911	-0.57102	-0.69034	-0.70529	-0.70688
A1						
$H^2$	0.00000	0.00000	0.00347	0.09098	-0.47162	-0.49119
HL	1.00000	1.00000	0.99981	0.99088	0.74351	0.71913
$L^2$	0.00000	0.00000	0.00051	0.09747	-0.47408	-0.49150
A2						
$H^2$	0.14751	0.27911	0.57101	0.68405	0.52441	0.50834
HL	0.00000	0.00001	0.00614	-0.13471	0.66871	0.69487
$L^2$	0.98906	0.96026	0.82092	0.71689	0.52707	0.50865

## 4 X-PAH<sub>n</sub>-Et-Au

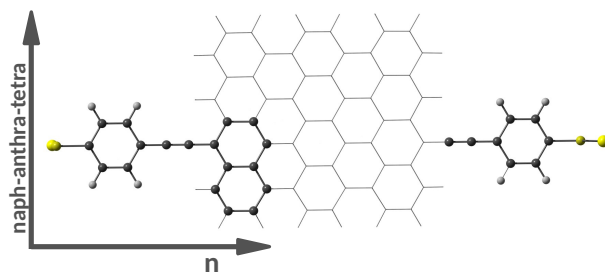


Figure S4: Schematic representation of the molecular junction X-PAH<sub>n</sub>-Et-Au

The same analysis performed for the model system in the body of the letter has been repeated for some of the “anti-Ohmic” molecular junctions proposed by Stuyver and co-workers.<sup>1</sup> This is the case of PAHs connected to gold by ethynylphenylthiol linkers (X-PAH<sub>n</sub>-Et-Au). In the letter, the reversed exponential decay has been found to be inherent to the PAH, therefore, the effect of the linker on this behavior (favorable, disfavorable or null) must be evaluated. For this reason, molecular junctions of X-PAH<sub>n</sub>-Et-Au are constructed as shown in Figure S4 and optimized at the B3LYP/cc-pVDZ level with LANL2DZ for gold atom.

### 4.1. Wavefunction stability and energy differences between singlet and triplet states for X-PAH<sub>n</sub>-Et-Au

Table S6: Stability (S) and Instability (I) of the wavefunction calculated with B3LYP/cc-pVDZ for X-PAH<sub>n</sub>-Et-Au

$n$	1	2	3
naphthalene (N)	S	S	S
anthracene (A)	S	I	I
tetracene (T)	S	I	I

Table S7: Triplet-singlet splitting (in kcal/mol) for X-PAH<sub>n</sub>-Et-Au calculated at the B3LYP/cc-pVDZ level

$n$	1	2	3
naphthalene (N)	42.08	31.36	23.59
anthracene (A)	30.37	11.24	-0.11
tetracene (T)	21.00	-0.72	-12.44

The wavefunction stability of the optimized X-PAH<sub>n</sub>-Et-Au treated with B3LYP/cc-pVDZ with LANL2DZ for gold atom are collected in Table S6. In Table S7, the triplet-singlet state energy differences are shown.

## 4.2. Conductance and transmission calculations of the X-PAH<sub>n</sub>-Et-Au

The electrical conductance was calculated using Electron Deformation Orbitals (EDOs) upon a bias voltage of 2V applied between the electrodes, and collected in Figure S5. Naphthalene displays an almost constant value of the conductance whereas for anthracene and tetracene increases as the system grows. The conductance also increases with the size of the fundamental unit (tetracene > anthracene > naphthalene).

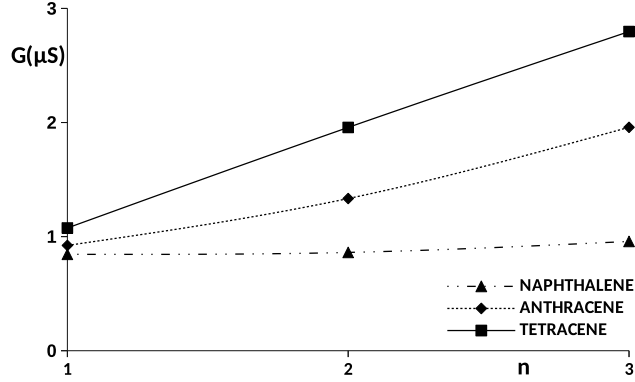


Figure S5: Evolution of the electrical conductance  $G$ , calculated within the EDOs formalism under a bias voltage of 2V, *vs* the number of fundamental units,  $n$ , for X-PAH<sub>n</sub>-Et-Au

In the work performed by Stuyver and co-authors,<sup>1</sup> the electrode representation was a six-atom triangular face-centered cubic (fcc) gold (111) surface, in this work it is just one gold atom. Also, their electronic transmission calculations were performed using NEGF-DFT by means of the Artaios code.<sup>2</sup> Then, to evaluate the possible variations arising from the different representations of the electrode, similar calculations were performed for the structures considered in this work and represented in Figure S6. Herein, for all the series, the transmission profiles match, both in shape and tendency, those obtained by the cited authors, evidencing the rising tendency of the transmission with the length and the decrease of the energy gap. Therefore, it can be concluded that the simpler electrode model employed in this work does not condition the results.

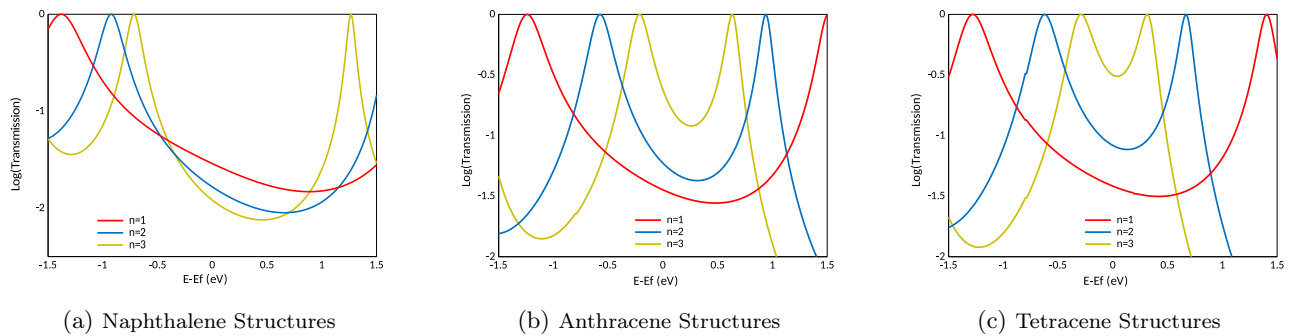


Figure S6: Electron Transmission calculated with NEGF-DFT for X-PAH<sub>n</sub>-Et-Au

### 4.3. Kohn-Sham orbital band of the X-PAH<sub>n</sub>-Et

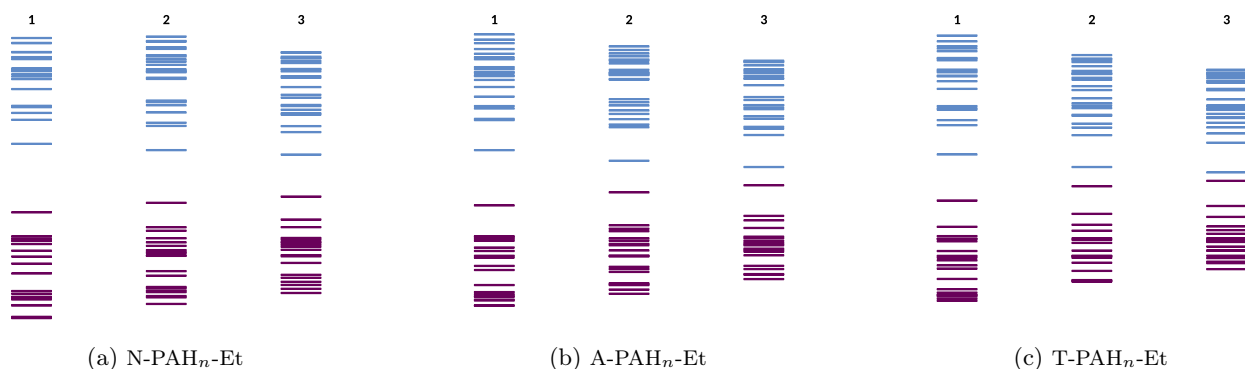


Figure S7: Kohn-Sham orbital bands representation of X-PAH<sub>n</sub>-Et with n=1-3 within an energy window spanning of (-0.4)-(0.1) au

The orbital bands for the X-PAH<sub>n</sub>-Et are represented in Figure S7, evidencing the reduction of the HOMO-LUMO energy gap as the structure grows. In this case, the system does not get enough length to reach the HOMO-LUMO orbital degeneracy. Again, the energy difference between the HOMO(-1)-HOMO orbitals and the LUMO-LUMO(+1) orbitals is significant and remains almost constant.

### 4.4. Localization tensor (LT) of the X-PAH<sub>n</sub>-Et

The values of the LT for the X-PAH<sub>n</sub>-Et are represented in Figure 8. These values were calculated between the sides of the molecule, with the contributions of the atoms belonging to the linkers and edges of the central PAH unit. The LT for the structures containing just one fundamental unit are also shown in the figure, however, they are senseless for explaining long-range delocalization since they involve also pairs of atoms covalently bonded. It can be said that the LT obtained at DFT level reflects the increasing conductance with the number of units. The LT calculated using CASSCF(14,14) and CASSCF(2,2) evidence the normal exponential decay in the ground state, displaying an opposite trend to the DFT results.

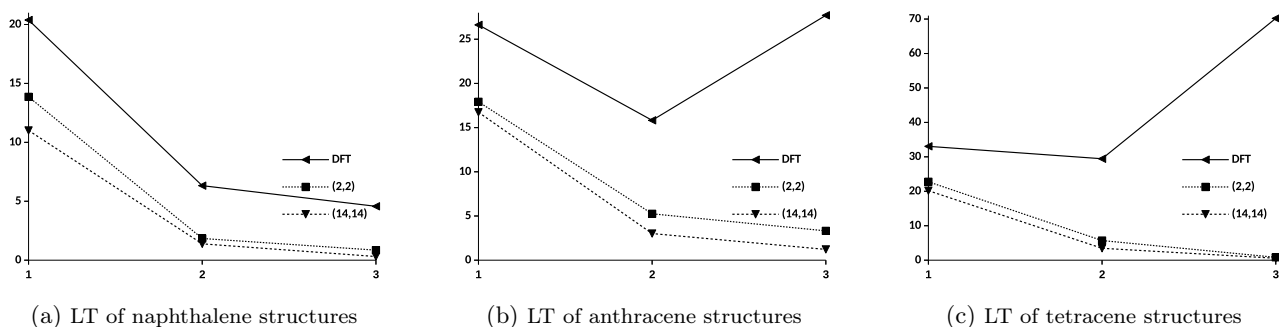


Figure S8: Evolution of the edge-to-edge interatomic localization tensor component ( $\Lambda^{AB}/au$ ) vs the number of fundamental units in X-PAH<sub>n</sub>-Et at DFT, CASSCF(2,2) and CASSCF(14,14) levels

## 4.5. CASSCF calculations of X-PAH<sub>n</sub>-Et

Single point (SP) calculations of the ground state (X) were performed with CASSCF(14,14)/cc-pVDZ and CASSCF(2,2)/cc-pVDZ level of theory for all X-PAH<sub>n</sub>-Et. Table S8 and Table S9 contain the relative weights of the most important configurations. Again, for those systems in which an instability of the wavefunction was found at DFT level, both configurations, the doubly occupied HOMO (H<sup>2</sup>) and the doubly occupied LUMO (L<sup>2</sup>), are relevant. This is the same as previously found for X-PAH<sub>n</sub>, *ie*, for the same systems without linker.

Table S8: Weight of the (H<sup>2</sup>) and (L<sup>2</sup>) configurations of state X at CASSCF(2,2) of X-PAH<sub>n</sub>-Et

<i>n</i>	1	2	3
naphthalene (N)			
H <sup>2</sup>	0.97206	0.97236	0.97262
L <sup>2</sup>	0.02794	0.02764	0.02738
anthracene (A)			
H <sup>2</sup>	0.96107	0.95397	0.76376
L <sup>2</sup>	0.03893	0.04603	0.23624
tetracene (T)			
H <sup>2</sup>	0.95418	0.78297	0.53841
L <sup>2</sup>	0.04582	0.21703	0.46159

Table S9: Weight of the (H<sup>2</sup>) and (L<sup>2</sup>) configurations of state X at CASSCF(14,14) of X-PAH<sub>n</sub>-Et

<i>n</i>	1	2	3
naphthalene (N)			
H <sup>2</sup>	0.79004	0.79208	0.77943
L <sup>2</sup>	0.00913	0.00994	0.00352
anthracene (A)			
H <sup>2</sup>	0.78106	0.78887	0.52480
L <sup>2</sup>	0.02137	0.03117	0.26452
tetracene (T)			
H <sup>2</sup>	0.76349	0.60202	0.42600
L <sup>2</sup>	0.03218	0.17749	0.38307

## 4.6. Kohn-Sham orbital representation of X-PAH<sub>n</sub>-Et

The HOMO-LUMO orbitals are represented in Figures S9-S11. The representations show an increase of the orbital localization at the edges with the molecular size.



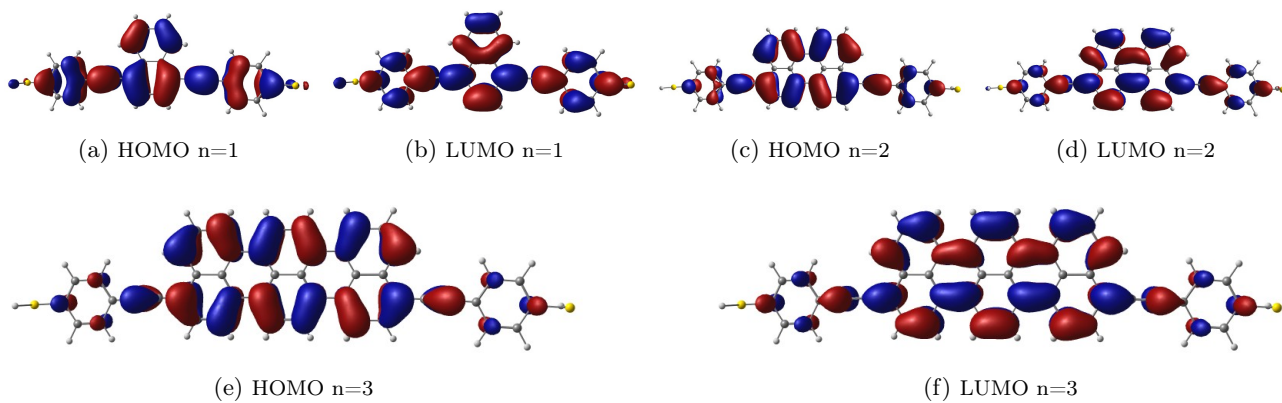


Figure S9: Kohn-Sham frontier orbitals of N-PAH<sub>*n*</sub>-Et, Isosurface value=0.02

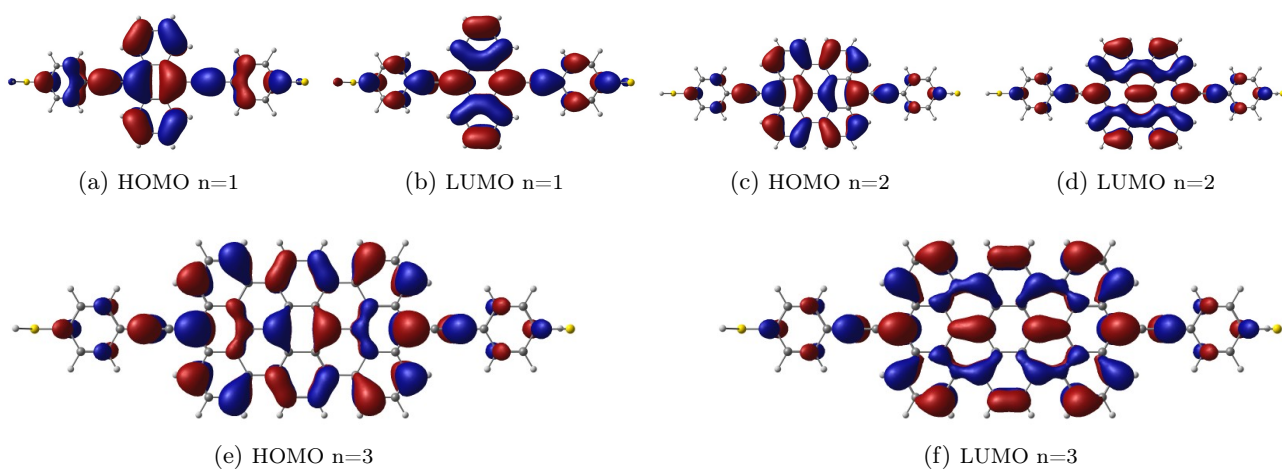


Figure S10: Kohn-Sham frontier orbitals of A-PAH<sub>*n*</sub>-Et, Isosurface value=0.02

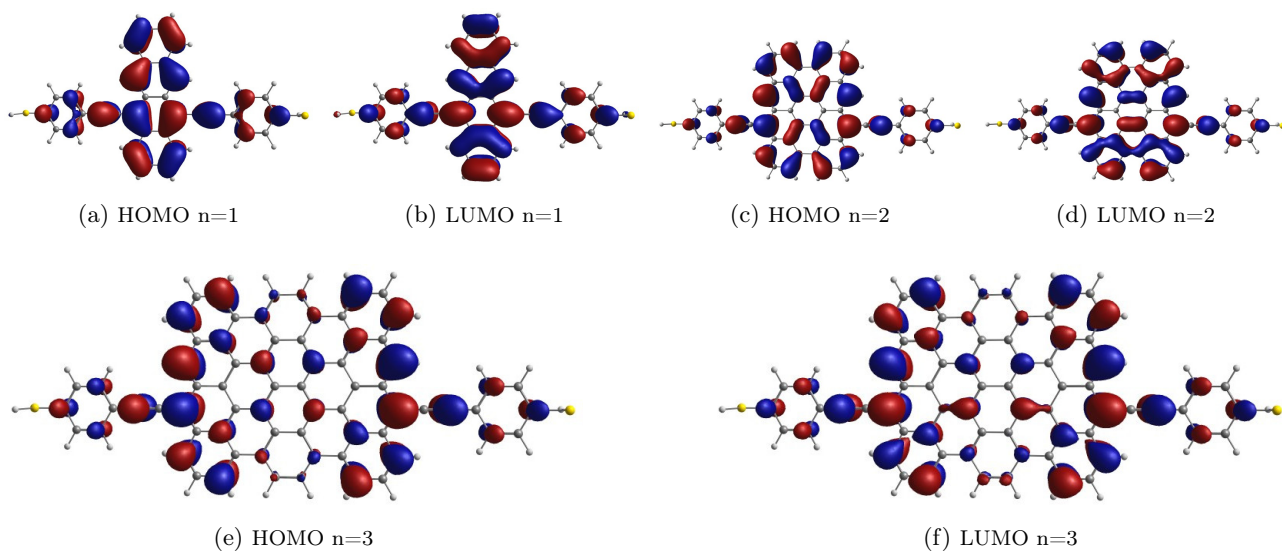


Figure S11: Kohn-Sham frontier orbitals of T-PAH<sub>*n*</sub>-Et, Isosurface value=0.02



## 5 Cum<sub>n</sub>-Am-Au and QDC<sub>n</sub>-Am-Au

Cumulenes and Quinoid-cumulenes (QDC) were also proposed as systems in which the exponential decay of the conductance with the length does not occur. Garner *et al.*<sup>7</sup> showed that, in this linear conjugated molecules, the bond-length alternation favors the reverse exponential decay. Again, to verify this, the study of cumulene and QDC structures was performed. These molecular junctions were constructed as shown in Figure S12 and S13 containing from  $n=1$  to  $n=9$  and from  $n=1$  to  $n=5$  intermediate units, respectively, with amine groups as linkers to the gold electrode, Cum<sub>n</sub>-Am-Au and QDC<sub>n</sub>-Am-Au. The same level of theory employed previously by Garner *et al.*<sup>7</sup> has been used here.

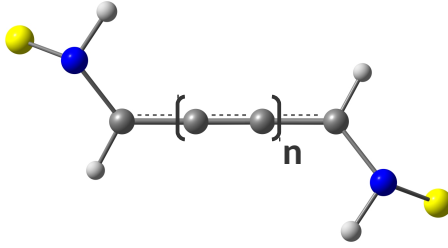


Figure S12: Schematic representation of the molecular junction: Cum<sub>n</sub>-Am-Au

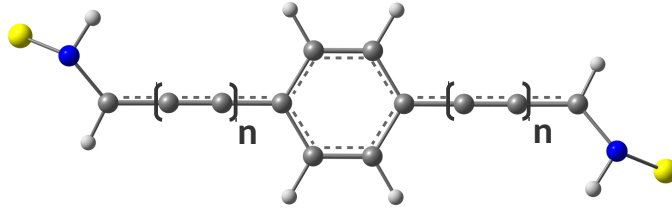


Figure S13: Schematic representation of the molecular junction: QDC<sub>n</sub>-Am-Au

### 5.1. Wavefunction stability and energy differences between singlet and triplet states of the Cum<sub>n</sub>-Am-Au and QDC<sub>n</sub>-Am-Au

Table S10: Stability (S) and Instability (I) of the wavefunction and triplet-singlet splitting (in kcal/mol) calculated with PBE/cc-pVDZ for Cum<sub>n</sub>-Am-Au

n	1	2	3	4	5	6	7	8	9
Stability	S	S	I	I	I	I	I	I	I
ΔE(S-T)	-5.24	-4.20	-3.70	-3.15	-2.69	-2.29	-1.96	-1.67	-1.42

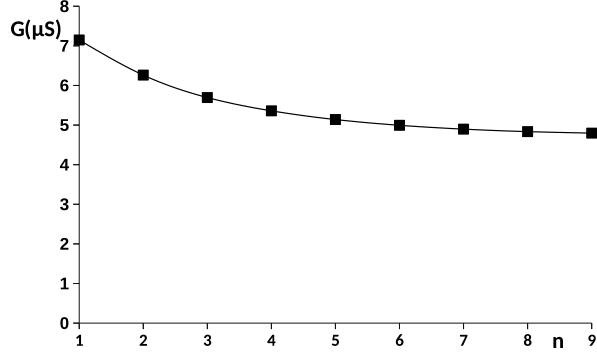
Table S11: Stability (S) and Instability (I) of the wavefunction and triplet-singlet splitting (in kcal/mol) calculated with PBE/cc-pVDZ for QDC<sub>n</sub>-Am-Au with  $n=1-5$

n	1	2	3	4	5
Stability	I	I	I	I	I
ΔE(S-T)	0.25	0.91	1.33	1.65	1.89

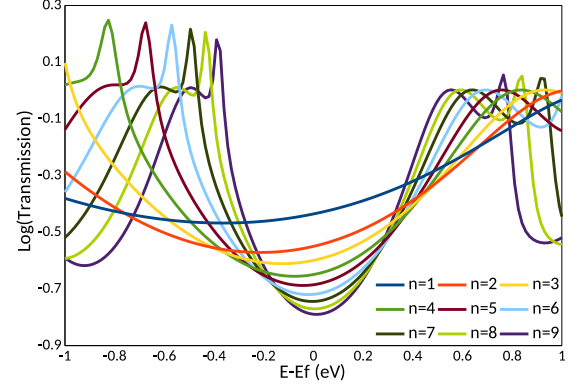
The wavefunction stability of the optimized Cum<sub>n</sub>-Am-Au and QDC<sub>n</sub>-Am-Au treated with PBE/cc-PVDZ

with LANL2DZ for gold atoms are shown in Table S10 and S11, respectively, so as the singlet and triplet state energy difference. The level of calculation selected was the same employed in previous works for these systems.<sup>7</sup>

## 5.2. Conductance and transmission calculations of $\text{Cum}_n\text{-Am-Au}$ and $\text{QDC}_n\text{-Am-Au}$

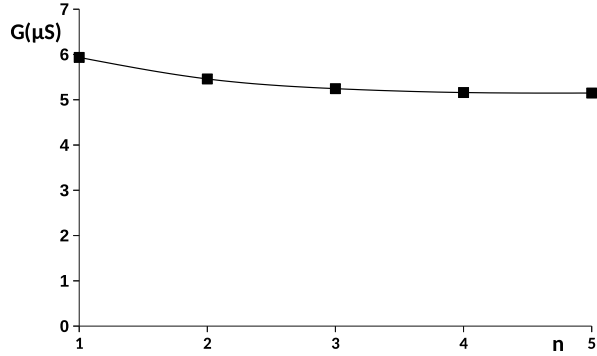


(a) Evolution of the electrical conductance  $G$ , calculated within the EDOs formalism under a bias voltage of 2V, *vs* the number of bonds,  $n$ , in  $\text{Cum}_n\text{-Am-Au}$

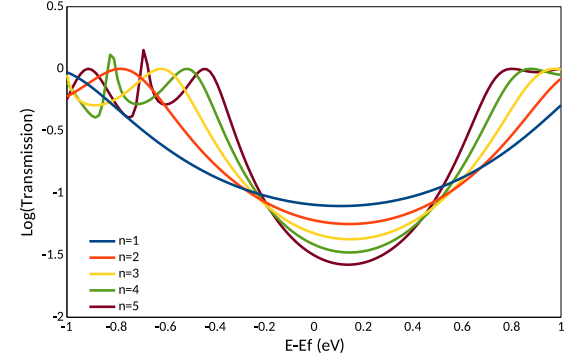


(b) Electron Transmission calculated with the NEGF-DFT formalism for  $\text{Cum}_n\text{-Am-Au}$

Figure S14: Conductance and Transmission of  $\text{Cum}_n\text{-Am-Au}$  series



(a) Evolution of the electrical conductance  $G$ , calculated within the EDOs formalism under a bias voltage of 2V, *vs* the number of bonds,  $n$ , in  $\text{QDC}_n\text{-Am-Au}$



(b) Electron Transmission calculated with the NEGF-DFT formalism for  $\text{QDC}_n\text{-Am-Au}$

Figure S15: Conductance and Transmission of the  $\text{QDC}_n\text{-Am-Au}$  series

The electrical conductance was calculated upon a bias voltage of 2V applied between the gold electrodes and represented in Figure S14(a) for  $\text{Cum}_n\text{-Am-Au}$  and Figure S15(a) for  $\text{QDC}_n\text{-Am-Au}$ . In addition, the electron transmission was calculated using the NEGF-DFT approach with the Artaios code<sup>2</sup> and represented in Figure S14(b) for  $\text{Cum}_n\text{-Am-Au}$  and Figure S15(b) for  $\text{QDC}_n\text{-Am-Au}$ . All plots reflect the same result: the conductance neither increases with the length nor shows an exponential decay, but reaches a constant and significantly large value for long chains. This is in agreement with the previous results obtained by Garner *et al.*<sup>7</sup> Anyway, the asymptotic behavior of the conductance at short and medium lengths allows glimpsing that the reversed exponential decay could arise at larger lengths.

## 5.3. Kohn-Sham orbital bands representation of $\text{Cum}_n\text{-Am}$ and $\text{QDC}_n\text{-Am}$

The orbital bands for the series of  $\text{Cum}_n\text{-Am}$  and  $\text{QDC}_n\text{-Am}$  are represented in Figure S16. The evidence the reduction of the energy gap as the system grows, although, in this case, the orbital energy profile does not meet the common orbital picture expected for this kind of systems. This is the reason why in the  $\text{Cum}_n\text{-Am}$  and  $\text{QDC}_n\text{-Am}$  series the conductance do not increases with the chain length.

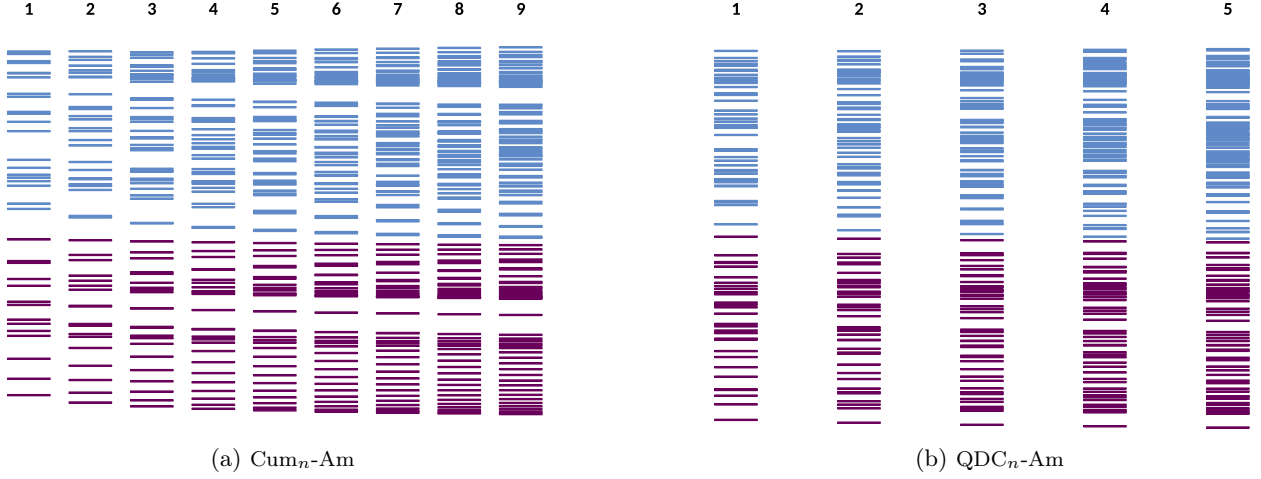


Figure S16: Kohn-Sham orbital bands representation of  $\text{Cum}_n\text{-Am}$  with  $n=1-9$  and  $\text{Cum}_n\text{-Am}$  with  $n=1-5$  respectively, within an energy window spanning of  $(-0.8)-(0.5)$  au

#### 5.4. Localization tensor (LT) of $\text{Cum}_n\text{-Am}$ and $\text{QDC}_n\text{-Am}$

In Figure S17(a), for  $\text{Cum}_n\text{-Am}$ , and S17(b), for  $\text{QDC}_n\text{-Am}$ , the values of the LT between nitrogen atoms are represented. At the DFT level, the LT evidences that the QDC and cumulene series have a conducting nature even at large distances. However, the LT calculated using CASSCF(14,14) reflect, as found for the previous systems, a systematic decrease of the electron transport ability with the chain length. So, the DFT results seem to be influenced, again, by the incorrect description of the wave function at single-reference level.

#### 5.5. CASSCF calculation of $\text{Cum}_n\text{-Am}$ and $\text{QDC}_n\text{-Am}$

Single point (SP) calculations of the ground state (X) were performed with CASSCF(14,14)/cc-pVDZ level of theory for the series of  $\text{Cum}_n\text{-Am}$  and  $\text{QDC}_n\text{-Am}$ . Table S12 and S13 contain the relative weights of the most important configurations.

Table S12: Weight of the ( $\text{H}^2$ ) and ( $\text{L}^2$ ) configurations of state X at CASSCF(14,14) of  $\text{Cum}_n\text{-Am}$

$n$	1	2	3	4	5	6	7	8	9
$\text{H}^2$	0.84500	0.76490	0.68896	0.69013	0.73382	0.70787	0.76668	0.74854	0.79162
$\text{L}^2$	0.04594	0.05405	0.06243	0.05477	0.02124	0.04294	0.04033	0.03690	0.02701

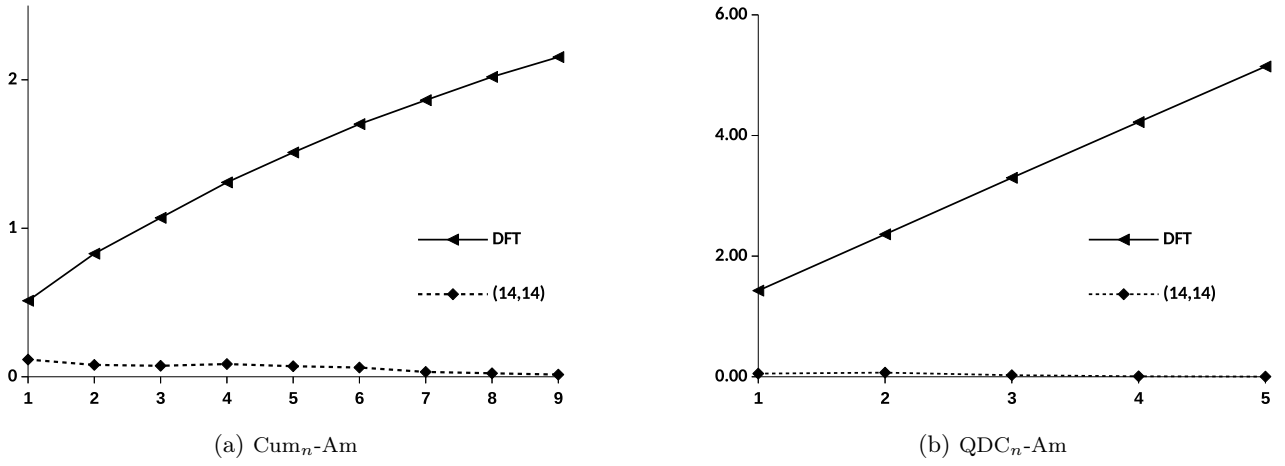


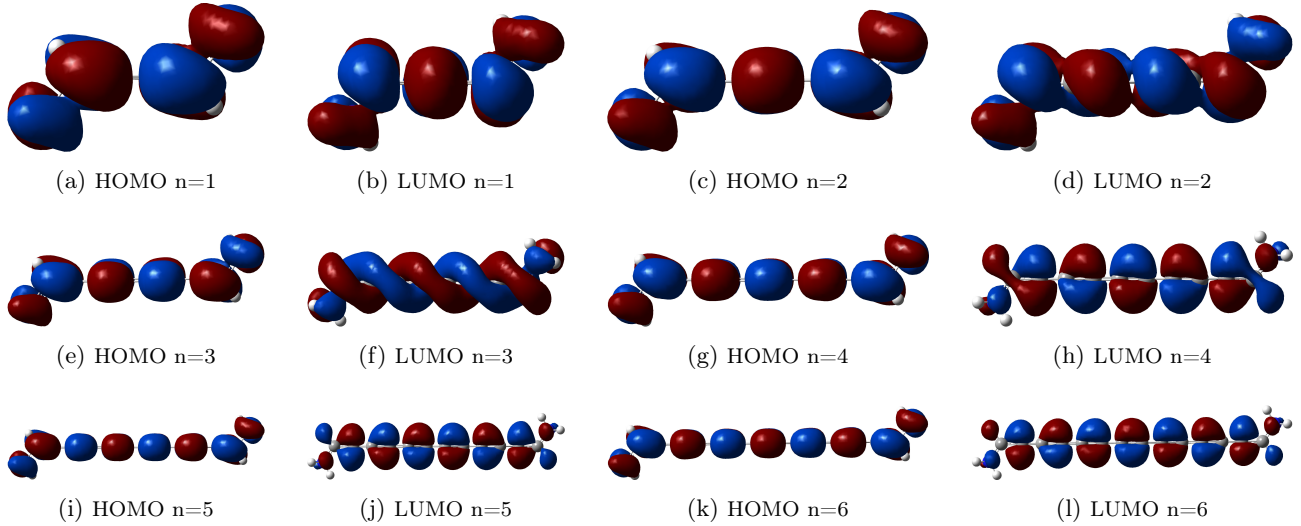
Figure S17: Evolution of the edge-to-edge interatomic localization tensor component ( $\Lambda^{AB}/au$ ) vs the number of bonds in Cum<sub>n</sub>-Am (a) and QDC<sub>n</sub>-Am (b) at DFT and CASSCF(14,14) levels

Table S13: Weight of the ( $H^2$ ) and ( $L^2$ ) configurations of state X at CASSCF(14,14) of QDC<sub>n</sub>-Am

$n$	1	2	3	4	5
$H^2$	0.64720	0.64964	0.46830	0.42416	0.40829
$L^2$	0.10275	0.14495	0.36716	0.38197	0.38245

## 5.6. Kohn-Sham orbital representation of Cum<sub>n</sub>-Am and QDC<sub>n</sub>-Am

The HOMO-LUMO orbitals are represented in Figures S18 and S19. These representations do not show orbital localization at the edges of the molecules with the molecular size.



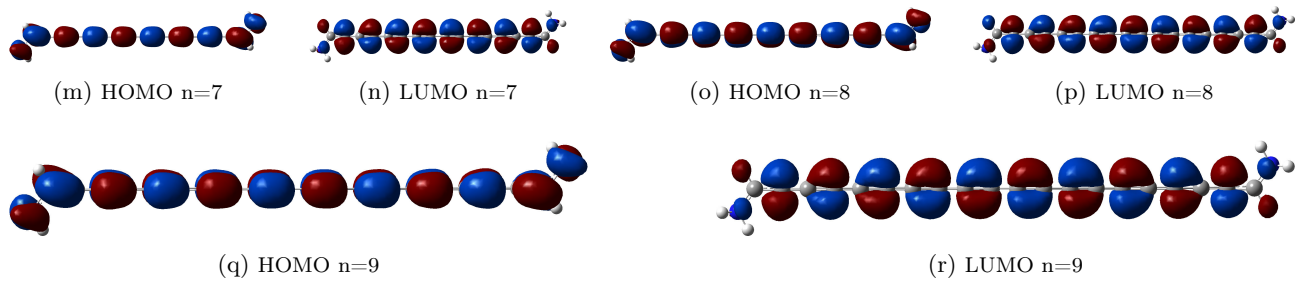


Figure S18: Kohn-Sham frontier orbitals of  $\text{Cum}_n\text{-Am}$ , Isosurface value=0.02

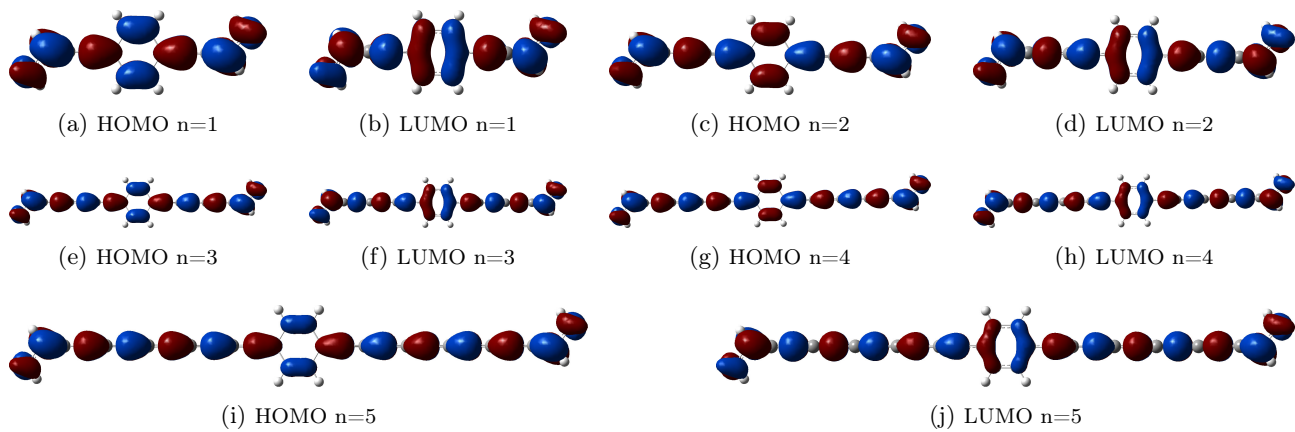


Figure S19: Kohn-Sham frontier orbitals of  $\text{QDC}_n\text{-Am}$ , Isosurface value=0.02

# References

- (1) Stuyver, T.; Zeng, T.; Tsuji, Y.; Geerlings, P.; De Proft, F., *Nano Lett.*, **2018**, *18*, 7298-7304.
- (2) Deffner, M.; Gross, L.; Steenbock, T.; Voigt, B. A.; Solomon, G. C.; Herrmann, C. ARTAIOS available from <https://www.chemie.uni-hamburg.de/ac/herrmann/software/index.html>.
- (3) Kohn, W.; *Phys. Rev.*, **1964**, *133*, A171–A181.
- (4) Resta, R. *Phys. Rev. Lett.*, **1998**, *80*, 1800–1803.
- (5) Pendás, Á. M.; Guevara-Vela, J. M.; Crespo, D. M.; Costales, A.; Francisco, E.; *Phys. Chem. Chem. Phys.*, **2017**, *19*, 1790–1797.
- (6) Gil-Guerrero, S.; Ramos-Berdullas, N.; Martín Pendás, Á.; Francisco, E.; Mandado, M. *Nanoscale Advances*, **2019**, *1*, 1901–1913.
- (7) Garner, M. H.; Bro-Jorgensen, W.; Pedersen, P. D.; Solomon, G. C., *J. Phys. Chem. C*, **2018**, *122*, 26777-26789.